J. Fluid Mech. (2011), *vol.* 685, *pp.* 335–364.
doi:10.1017/jfm.2011.319

Length of near-wall plumes in turbulent convection

Baburaj A. Puthenveettil[1]†, G. S. Gunasegarane[1], Yogesh K. Agrawal[2], Daniel Schmeling[3], Johannes Bosbach[3] and Jaywant H. Arakeri[4]

[1] Department of Applied Mechanics, Indian Institute of Technology Madras, Chennai, 600036, India

[2] Department of Mechanical Engineering, National Institute of Technology, Durgapur, 713209, India

[3] Institute of Aerodynamics and Flow Technology, German Aerospace Center (DLR), Göttingen, 37073, Germany

[4] Department of Mechanical Engineering, Indian Institute of Science, Bangalore, 560012, India

(Received 2 April 2011; revised 13 June 2011; accepted 19 July 2011; first published online 20 September 2011)

We present planforms of line plumes formed on horizontal surfaces in turbulent convection, along with the length of line plumes measured from these planforms, in a six decade range of Rayleigh numbers ($10^5 < Ra < 10^{11}$) and at three Prandtl numbers ($Pr = 0.7, 5.2, 602$). Using geometric constraints on the relations for the mean plume spacings, we obtain expressions for the total length of near-wall plumes on horizontal surfaces in turbulent convection. The plume length per unit area (L_p/A), made dimensionless by the near-wall length scale in turbulent convection (Z_w), remains constant for a given fluid. The Nusselt number is shown to be directly proportional to L_pH/A for a given fluid layer of height H. The increase in Pr has a weak influence in decreasing L_p/A. These expressions match the measurements, thereby showing that the assumption of laminar natural convection boundary layers in turbulent convection is consistent with the observed total length of line plumes. We then show that similar relationships are obtained based on the assumption that the line plumes are the outcome of the instability of laminar natural convection boundary layers on the horizontal surfaces.

Key words: buoyant boundary layers, plumes/thermals, turbulent convection

1. Introduction

In turbulent natural convection over horizontal surfaces, rising sheets of hot fluid, often called ‘line plumes’ due to their appearance as lines in the top views, are the commonly observed coherent structures near the hot horizontal plate (Husar & Sparrow 1968; Tamai & Asaeda 1984; Zocchi, Moses & Libchaber 1990; Theerthan & Arakeri 2000; Haramina & Tilgner 2004; Funfschilling & Ahlers 2004; Puthenveettil & Arakeri 2005; Zhou, Sun & Xia 2007; Zhou & Xia 2010). These line plumes form and merge all over the surface, resulting in a complex pattern of near-wall coherent structures at any instant. Since these plumes transport the major part of the heat from the plate (Shishkina & Wagner 2007), quantifying these structures is of importance in understanding the heat flux scaling in turbulent convection. The present study proposes

† Email address for correspondence: apbraj@iitm.ac.in

relations for the length of these line plumes to the driving potential and the heat flux in turbulent convection.

We define the Rayleigh number as $Ra = g\beta\Delta TH^3/\nu\alpha$ and the Prandtl number as $Pr = \nu/\alpha$. Here, g denotes the acceleration due to gravity, β the coefficient of thermal expansion, ΔT the temperature difference across the fluid layer, H the height of the fluid layer, ν the kinematic viscosity and $\alpha = k/\rho C_p$ the thermal diffusivity with k the thermal conductivity, ρ the density and C_p the specific heat at constant pressure. The Rayleigh number based on the near-wall temperature drop, defined as

$$Ra_w = g\beta\Delta T_w H^3/\nu\alpha, \tag{1.1}$$

is equal to $Ra/2$ since the near-wall temperature drop ΔT_w is equal to $\Delta T/2$ at high Ra; Ra_w is the Rayleigh number used in open convection systems. Hereafter, the term 'wall' is used to refer to the top or bottom horizontal surfaces that confine the fluid layer and not to the vertical bounding surfaces. The Nusselt number, $Nu = Q/(k\Delta T/H)$ is a function of Ra and Pr, where Q is the heat flux. These definitions also hold for concentration driven convection if the concentration difference across the fluid layer ΔC replaces ΔT, the molecular diffusivity D replaces ν, the Schmidt number Sc replaces Pr, q_m the mass flux replaces the kinematic heat flux $q = Q/\rho C_p$ and Sh the Sherwood number replaces Nu.

At high Ra, the fluid layer divides into bulk and near-wall regions which respectively have predominantly turbulent and diffusive transport (Adrian, Ferreira & Boberg 1986; Theerthan & Arakeri 1998, hereafter referred to as TA; Puthenveettil & Arakeri 2005, hereafter referred to as PA). The near-wall region, being diffusive, offers the predominant resistance to the transport of heat and hence mostly determines the flux scaling. In these near-wall regions, line plumes are initiated. The line plumes have a finite thickness and a finite height, beyond which they breakup into mushroom type plumes. Owing to their finite volume, they are also termed as rod-like plumes (Zhou & Xia 2010) or sheet plumes (PA). The line plumes elongate and merge with the adjacent sheets, a new sheet being initiated in the space vacated by the merger. The external shear due to the large-scale circulation modifies these dynamics by aligning the sheets in the direction of the shear (Theerthan & Arakeri 2000; PA). Puthenveettil, Ananthakrishna & Arakeri (2005) found that the plume structure at any instant caused by these dynamics had a common fractal nature, independent of Ra over a decade (10^{10}–10^{11}) of Ra. This common fractal nature at all Ra, which showed that the probability of occurrence of a line plume in any area of the horizontal surface was independent of Ra, implied that there is some commonality in the dynamics of plume merging at all Ra. However, the plumes merged faster with increase in Ra (Gunasegarane & Puthenveettil 2010) and the mean ($\overline{\lambda}$) of the spacings between the line plumes (λ) at any instant decreased with increase in Ra (TA; PA). Interestingly, similar to the common fractal nature of the plume structure, these plume spacings were also distributed as a common lognormal probability distribution function, independent of Ra (PA).

Since the planforms of the plume structure at any instant had a lognormal distribution of spacings, with the variance of λ being of the same order as $\overline{\lambda}$ (PA; Puthenveettil & Arakeri 2008; Ramareddy & Puthenveettil 2011), a single mean spacing may not be a complete measure to characterize the structure; more representative, unique and integral measures to characterize the near-wall coherent structures are needed. The total length of plume lines on the surface could be expected to be more or less fixed for a given Ra or heat flux Q since it is an integral quantity. The lengths of the line plumes are easily and accurately measured compared

with the normal spacings between them even if the plumes are oriented randomly. Since the line plumes carry the major part of the heat flux, characterizing the plume structure in terms of plume length could lead to unique relations between the length of the near-wall coherent structures in turbulent convection and the driving potential or flux. Such relations could be of great importance in building wall functions for turbulence modelling of convection, since these plumes, by their dynamics, and by the entrainment velocity field they engender, predominantly determine the near-wall velocity fields in turbulent convection. More importantly, if such relations are also predicted by a hypothesis about the near-wall coherent structures, the match of the predictions with the measurements is an evidence of the correctness of the phenomenology.

In this paper, we propose relations for the total length of line plumes on horizontal walls in turbulent convection, based on two formulations. These relations are shown to match the measurements from planforms obtained from our experiments, as well as from other investigators. Both formulations are related and have the underlying assumption that the boundary layers in turbulent convection are laminar natural convection boundary layers, which become unstable to give rise to line plumes. In other words, the near-wall region in turbulent convection may be considered as an ensemble of laminar, or more appropriately viscous line plumes; see the discussion in TA and PA. In the first formulation, a relation for the plume spacings, obtained by TA and PA by equating the heat carried away by laminar natural convection boundary layers over $\overline{\lambda}$ to experimental flux correlations, is subjected to geometrical constraints of finite plate size to obtain expressions for the length of line plumes. An alternate formulation where the heat carried away by laminar line plumes is equated to the heat flux from the plate, along with a stability condition for laminar natural convection boundary layers, gives similar relations as from the earlier formulation.

The paper is organized as follows. We first describe the experimental setups and the planforms that are obtained over a six decade range of Ra_w ($4.6\times10^5 < Ra_w < 2\times10^{11}$) and at Pr of 0.7, 5.2 and 602 in § 2. The methods employed for measuring the length of line plumes from these planforms are described in § 3. The relations for the total length of line plumes are obtained and verified with the measurements in § 4.1. The alternative formulation based on relating the heat carried away by the line plumes to the heat flux to the plate, is shown in § 4.2. In the work we describe here, the expressions for plume lengths were derived by B.A.P. and Y.K.A. The experiments were conducted by G.S.G. and B.A.P. with the help of D.S. and J.B. The measurements of plume lengths were conducted by Y.K.A., G.S.G. and B.A.P. The idea to study the plume lengths, as well as critical comments on the manuscript came from J.H.A. The manuscript was written by B.A.P.

2. The planforms of plume structure

Figures 1, 2 and 4 show the planforms obtained from our experiments that are analysed in the present work; we also analyse a few other planforms obtained by Shishkina & Wagner (2008) and Stevens, Verzicco & Lohse (2010) and Zhou & Xia (2010). The parameter values corresponding to all of the analysed planforms are specified in tables 1 and 2.

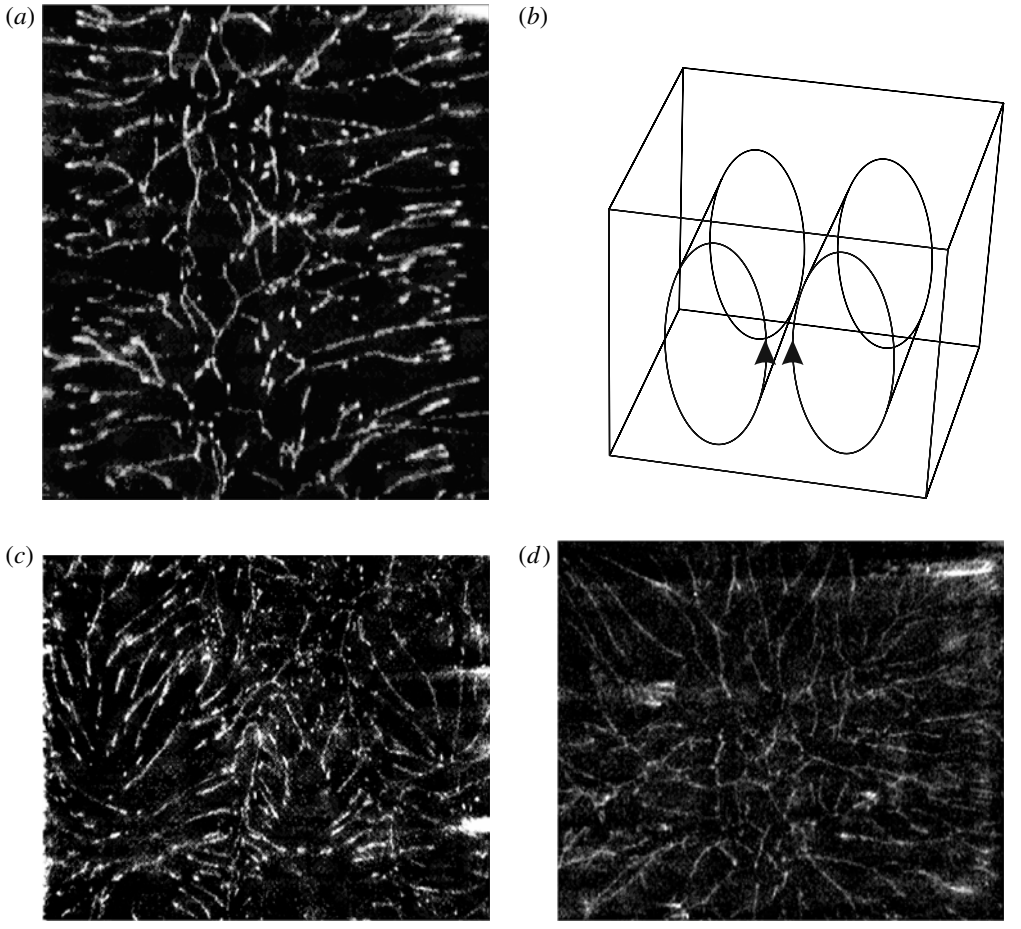

FIGURE 1. For caption see next page.

2.1. *Planforms at* $Sc = 602$

The planforms in figure 1 are taken from PA. The lines in the planforms are the top view of the line plumes rising from the horizontal surface. These images were obtained in quasi-steady concentration driven convection across a horizontal membrane of 0.45 μm mean pore size at $Sc = 602$ by placing a layer of brine over a layer of water separated by the membrane (PA). A schematic of the experimental setup is shown in figure 3(*a*). The membrane was needed since PA used concentration differences to drive the convection. The use of concentration difference helped PA to reach high Ra and Sc since the molecular diffusivity of salt in water is 100 times lower than the corresponding thermal diffusivity. As long as there was no flow across the membrane, which was ensured by using a membrane of small pore size, there will be only diffusive transport of salt across the membrane; the membrane behaved similar to a plate with finite conductivity in thermal convection. The convection was characterized by Ra_w, which was calculated by using the concentration drop above or below the membrane. The concentration drop above the membrane was obtained by deducting the diffusion concentration drop across the membrane from the total concentration drop between the tanks (PA). The total concentration drop was

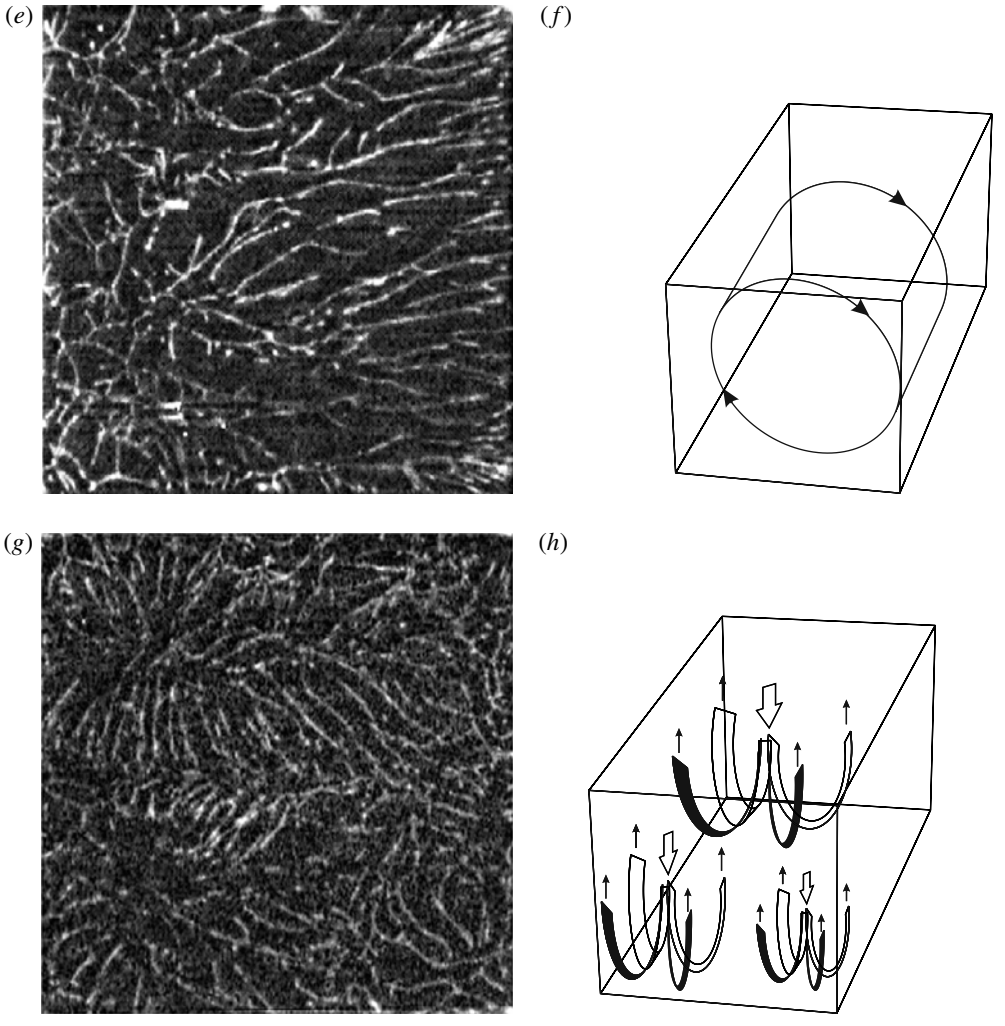

FIGURE 1. (cntd) Planforms of the plume structure in concentration driven convection in water at $Sc = 602$, obtained from PA. The white lines in the images are the top view of the line plumes just above the horizontal surface. The parameters corresponding to the planforms are shown in table 1. Here Ra_w increases from (*a*) to (*g*). (*a*), $Ra_w = 6.39 \times 10^{10}$; (*b*) schematic of the large-scale flow in (*a*); (*c*) $Ra_w = 1.667 \times 10^{11}$; (*d*) $Ra_w = 1.67 \times 10^{11}$; (*e*) $Ra_w = 2.03 \times 10^{11}$; (*f*) schematic of the large-scale flow in (*e*); (*g*), $Ra_w = 2.04 \times 10^{11}$; (*h*), schematic of the large-scale circulation in (*g*).

estimated by the transient measurements of conductivity in the top tank and then using mass balance (see PA for details). The experiments with the membrane were unsteady, but the time scales of variation of the bulk concentration and flux were much larger than the time scale of variation of the large-scale flow (PA; Puthenveettil & Arakeri 2008). Similarly the time scale of variation of the large scale flow was much larger than the time scale of near-wall dynamics (Ramareddy & Puthenveettil 2011). The near-wall dynamics were then essentially under constant flux, constant bulk concentration and constant large scale flow velocity as in steady Rayleigh–Bénard convection (RBC). The wide separation of time scales made the system quasi-steady

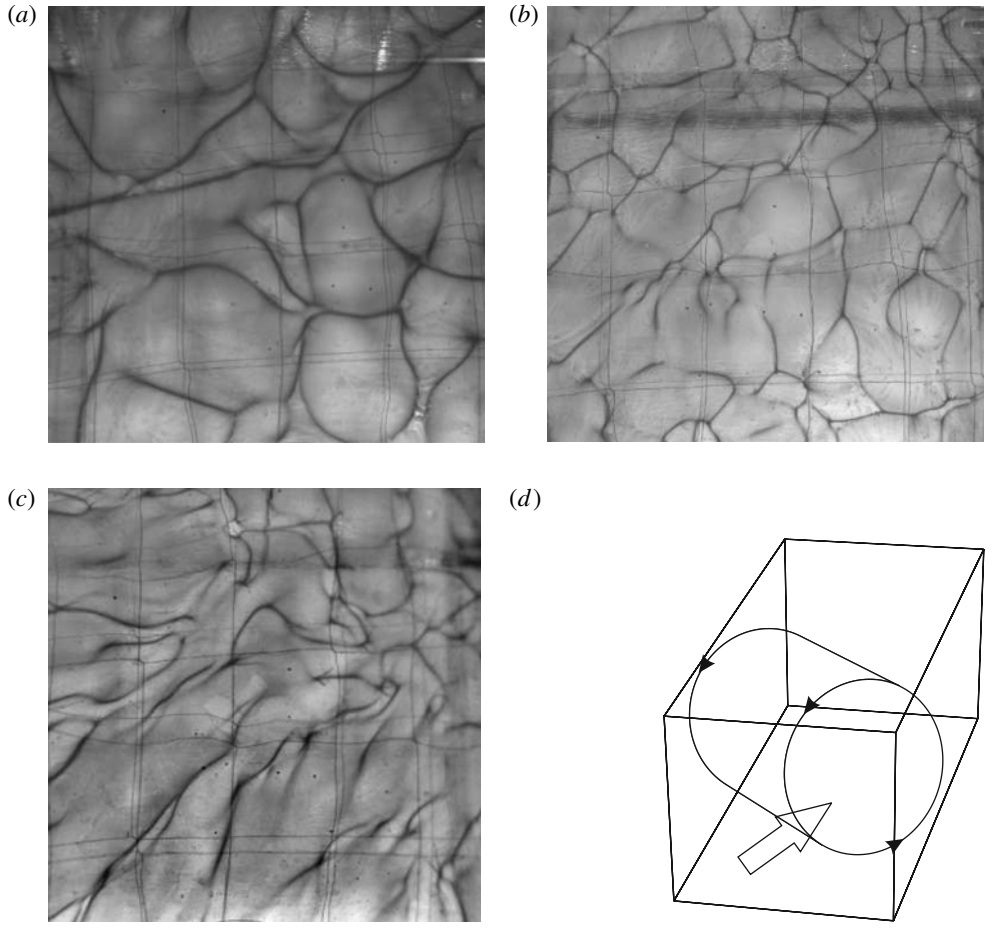

FIGURE 2. For caption see next page.

and hence comparable with steady convection systems such as RBC; the reader is referred to Puthenveettil & Arakeri (2005, 2008) and Ramareddy & Puthenveettil (2011) for details. Hence, the dynamics and the flux as a function of Ra_w was the same as that in temperature driven convection at the corresponding Pr and Ra_w.

The planform structure was visualized by the fluorescence of the dyed water from below the membrane intersecting an Ar ion laser (488 nm) sheet just above the membrane. Two aspect ratios, $\zeta = 0.65$ and 0.435, were used corresponding to tank cross sections of 15 cm × 15 cm (figures 1*a*, 1*c* and 1*g*) and 10 cm × 10 cm (figure 1*d* and 1*e*) for a fluid layer height of 23 cm. The flow structures were inferred from the alignment of the plumes caused by the large-scale flow and from the direction in which the plume heads were swept away by the large-scale flow. Figure 1(*a*) has two counter-rotating large-scale flow cells, counter clockwise on left and clockwise on right as shown in figure 1(*b*). Figure 1(*e*) has only a single large-scale flow cell rotating in the clockwise sense, see figure 1(*f*). Further details of the experimental setup, visualization procedure and the planforms could be found in PA and Puthenveettil *et al.* (2005) and Puthenveettil & Arakeri (2008).

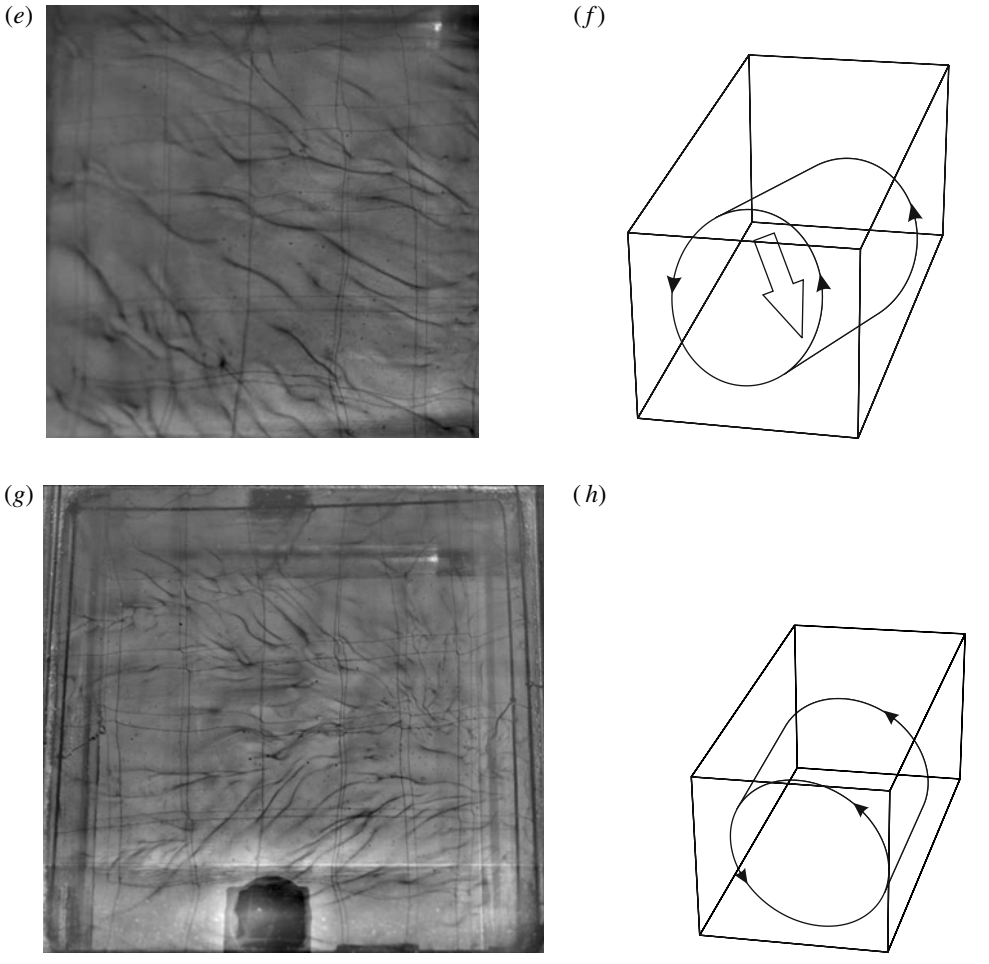

FIGURE 2. (cntd.) Planforms of plume structure in temperature driven convection in water at $Pr = 6$ observed just above the horizontal surface using electrochemical visualization. The thicker dark lines in the image are the top view of the line plumes, the thinner cross wires are the copper wires used as the anode. Here Ra_w increases from (*a*) to (*g*) as shown in table 1. (*a*) $Ra_w = 4.43 \times 10^5$; (*b*) $Ra_w = 3.95 \times 10^6$; (*c*) $Ra_w = 4.88 \times 10^7$; (*d*) schematic of large-scale flow in (*c*); (*e*) $Ra_w = 7.95 \times 10^8$; (*f*) schematic of the large-scale flow in (*e*); (*g*) $Ra_w = 1.06 \times 10^9$; (*h*) schematic of the large-scale flow in (*g*). The direction of near-wall shear is shown by the open arrow.

2.2. *Planforms at* $Pr = 5.2$

The images in figures 2 were obtained by electrochemical visualization (Baker 1966) in unsteady temperature driven convection in water in a 30 cm × 30 cm tank. As shown in figure 3(*b*), the water layer was heated from the bottom with various constant heat fluxes while its top surface was open to atmosphere, so that a steady ΔT_w was obtained. The heat flux was measured using the temperature drop T_1–T_2 across the glass plate in figure 3(*b*). For each *Ra*, the experiment was run for nearly 2 hours to ensure a constant ΔT_w condition inside the convection cell. The top and bottom boundaries of the cell are not in steady state, but the temperature difference across the fluid layer is, as the top and bottom boundaries become warmer at the same rate.

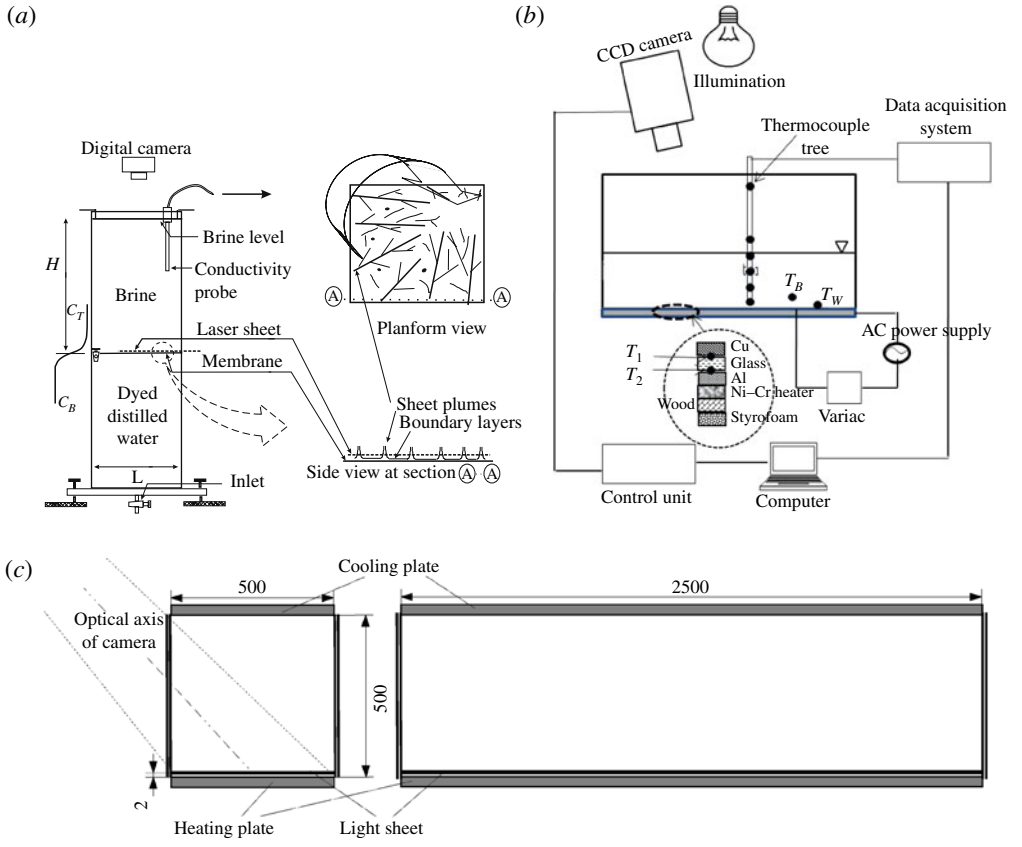

FIGURE 3. (Colour online available at journals.cambridge.org/flm) The experimental arrangements used to obtain the planforms; (*a*) the experimental setup for the concentration driven convection across a membrane; (*b*) the experimental setup for temperature driven convection in water; (*c*) the experimental setup for temperature driven convection in air.

Since the turbulence is decided by the temperature difference across the fluid layer and not by the temperatures of the bounding surfaces, the turbulent phenomena will be the same as in the corresponding steady situation at the same ΔT_w. To achieve $10^5 < Ra_w < 10^9$ at $Pr = 5.2$, the water layer height was changed from 5 cm to 20 cm so that $1.5 \leqslant \zeta \leqslant 6$. Owing to the local changes in pH near the hot plate, maintained as the cathode, thymol blue dye in water becomes darker near the hot plate, enabling us to see the local structures near the wall; the dark lines in the images are the near-wall plumes observed like this. The thin cross wires in the images are the copper wires used as the anode placed at some height from the hot plate. For further details, the reader is referred to Gunasegarane & Puthenveettil (2010). The planforms show that with increasing Ra, the polygonal structure breaks up into a structure composed of more aligned plumes. We expect this increasing alignment to be due to the increasing strength of the shear caused by a stronger large-scale flow at higher Ra_w. The lines in the images become weaker with increasing Ra_w as the line plumes are eroded more by the turbulent bulk with increasing Ra. We observe only a single large-scale flow cell as shown in figure 2(*d*,*f*,*h*), presumably due to the larger ζ compared with that in figure 1.

2.3. *Planforms at* $Pr = 0.7$

Figure 4 shows the planforms of plume structures observed in steady temperature driven convection of air confined between two 250 cm × 50 cm horizontal plates separated by 50 cm high double-walled polycarbonate plates. Figure 3(*c*) shows a schematic of the experimental setup. Isothermal boundary conditions were obtained by passing water from a temperature controlled heating system below the bottom aluminium plate, while the top plate was passively cooled by an air–air heat exchanger. Air mixed with smoke filled the cell. The structures are seen due to the scattered light from smoke particles when a 532 nm horizontal laser light sheet is passed grazing the bottom plate. Figure 4 shows only an area of ≈1 m × 50 cm on the left-hand side of the plate. Since the plumes are fed by the near-wall boundary layers which are relatively deficient of smoke particles, the plume regions appear as dark lines in a bright background. The images were obtained by viewing the horizontal laser sheet from the sides; the images were corrected for perspective errors. The perspective correction was obtained by calibrating the imaging arrangement with a horizontal grid on the bottom plate. Experiments with varying ΔT between the plates were conducted to obtain planforms for $1.3 \times 10^8 < Ra_w < 2.5 \times 10^8$.

3. Measurement of plume lengths

The plumes are detected first by the experimental techniques described in § 2. The methods employed for measuring the plume lengths only use an intensity criterion on the experimental image to classify some regions as plumes. It is hence important that the experimental techniques used in the study do not miss any plumes. In the planar laser-induced fluorescence (PLIF) technique used for the $Sc = 602$ experiments, since the fluorescent dye is present in a much larger concentration in all of the plume regions than in the background because only the bottom fluid is dyed, all of the plume regions fluoresce when a laser sheet is passed near the membrane. In the electrochemical technique used for the $Pr = 5.2$ study, since the pH changes uniformly near the bottom plate because of the uniform electrical field maintained by a grid type electrode, a layer of dark fluid forms uniformly on the bottom plate which is carried away by the boundary layers into the plumes. The plumes when they rise up change their colour back to the background fluid colour so that only the near-wall plumes are visible in the images. No plumes are missed by this technique. In the laser scattering technique used in the $Pr = 0.7$ study in air, smoke is introduced into the bulk, the system itself causes a relative deficiency of smoke particles in the plumes because the smoke particles have to get into the plumes through entrainment from the bulk. Owing to this, all of the plume regions will scatter less light when a laser sheet is passed near the bottom wall; all of the plumes in the laser path will appear darker. No plumes are likely to be missed here either. As seen in figures 1, 2 and 4 the plume regions are visually quite clear in the images obtained by such techniques.

The plume lengths were measured from such images in two ways:

(*a*) by an automated skeletonization image processing routine; and

(*b*) by manually covering the plumes with short linear segments.

For all of the images in figure 1 and for images in figure 2 that have good contrast and uniform background illumination, a skeletonization procedure was found to adequately represent the plume structure with lines. The images were first background corrected to remove non-uniform illumination. The edges in the images were then detected by the Canny edge detection routine (Canny 1986). The Canny edge detection routine

https://doi.org/10.1017/jfm.2011.319 Published online by Cambridge University Press

Figure	Ra_w (1.1)	Driving potential	Flux	Dimensionless flux	H (cm)	A_p (cm^2)	A (cm^2)	Image size (cm^2)	L_p (cm)	Pr
1(*a*)	6.39×10^{10}	1	0.021	270.03	23	15×15	225	13×14	401.1	602
1(*c*)	1.667×10^{11}	2.65	0.09	438.79	23	15×15	186.3	15×12	466.57	602
1(*d*)	1.67×10^{11}	2.62	0.08	394.5	23	10×10	79.8	9.6×9.87	233	602
1(*e*)	2.03×10^{11}	3.2	0.1094	441.7	23	10×10	86.49	9.57×9.76	232.61	602
1(*g*)	2.04×10^{11}	3.21	0.1116	449.18	23	15×15	225	14.25×14.54	610	602
2(*a*)	4.43×10^{5}	0.13	65	20.16	5	30×30	537.3	22×23.8	163	5.2
2(*b*)	3.95×10^{6}	1.16	585	20.33	5	30×30	560.74	23.3×23.6	353	5.2
2(*c*)	4.88×10^{7}	1.79	585	26.36	10	30×30	519.84	24.1×22.6	378	5.2
2(*e*)	7.95×10^{8}	3.65	2340	103.4	20	30×30	685.39	24.3×25.1	432	5.2
2(*g*)	1.06×10^{9}	4.87	4158	137.44	20	30×30	514.38	29.8×28.7	522	5.2
4(*a*)	1.287×10^{8}	10.48	19.12	35.22	50	250×50	4930	103.9×47.6	841	0.7
4(*b*)	1.766×10^{8}	15.46	31.44	38.73	50	250×50	4930	103.9×47.6	979	0.7
4(*c*)	2.183×10^{8}	20.17	44.16	41.27	50	250×50	4930	103.9×47.6	1080	0.7
4(*d*)	2.542×10^{8}	24.89	57.64	43.20	50	250×50	4930	103.9×47.6	1140	0.7

TABLE 1. Parameter values for the planforms shown in figures 1, 2 and 4. Figures 1(*a*)–(*g*) are for concentration driven convection and hence the flux is in mg cm^{-2} min^{-1}, the driving potential in g l^{-1} and the dimensionless flux is *Sh*. For the other entries these are respectively in W m^{-2}, °C and *Nu*. Here A is the actual area over which the length of plumes L_p is measured and A_p is the cross-sectional area of the convection cell. Owing to cropping of the images, sometimes needed to exclude non-plume objects in the analysis, the image size and A need not be equal to A_p.

https://doi.org/10.1017/jfm.2011.319 Published online by Cambridge University Press

Reference	Ra_w (1.1)	Driving potential ΔT_w (°C)	Flux (W m^{-2})	Nu	H (cm)	$A = A_p$ (cm^2)	L_p (cm)	Pr
Shishkina & Wagner (2008)	1×10^9	6.60	2886.2	81.0	20.0	314.2	108.4	5.4
Zhou & Xia (2010)	5.5×10^8	3.15	1339.5	64.5	18.5	269.0	182.3	5.4
Stevens *et al.* (2010)	1×10^9	5.00	16.35	79.75	126.6	3148	768.0	0.7

TABLE 2. Parameter values corresponding to the plume lengths of other investigators.

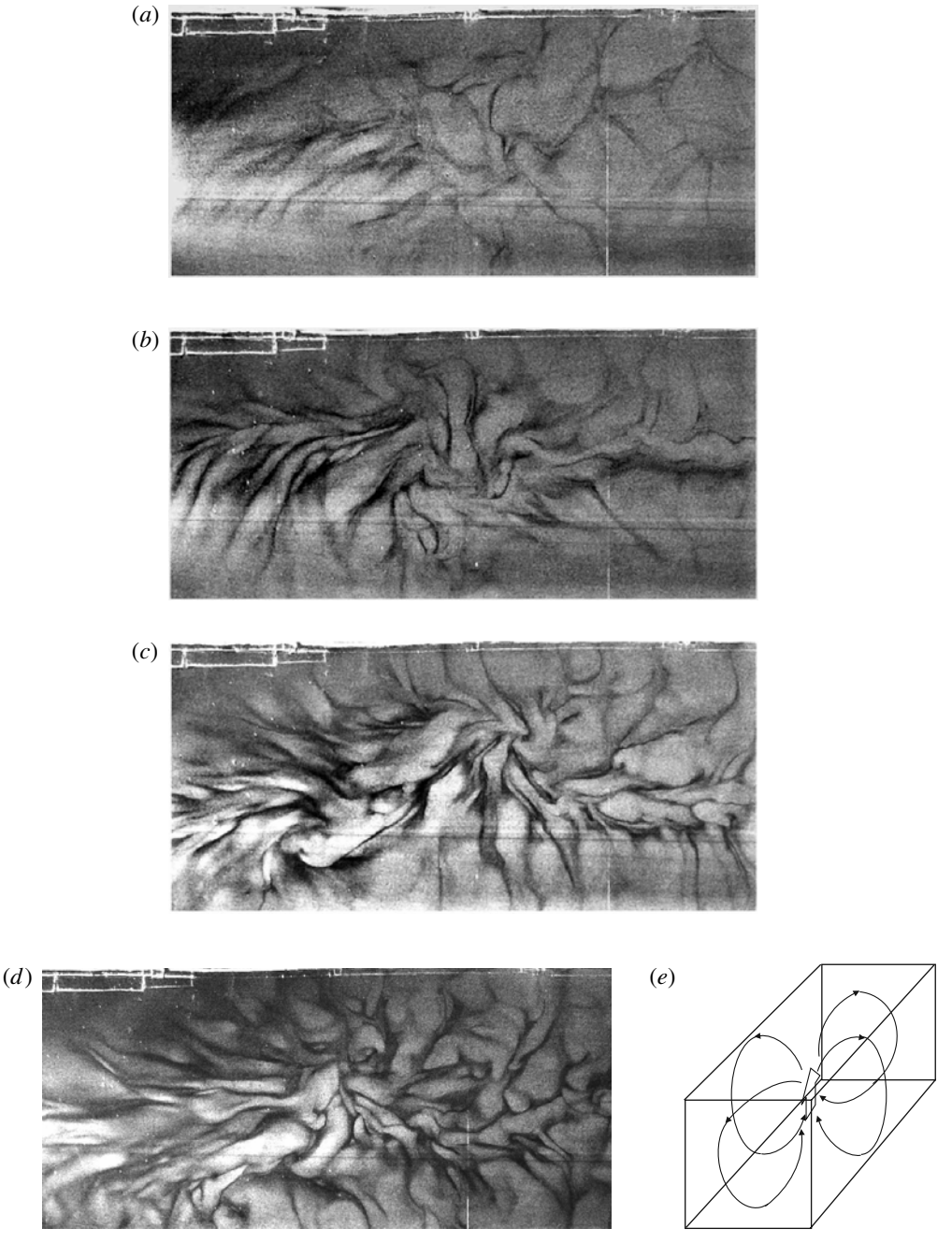

FIGURE 4. Planforms of plume structure, observed just above the bottom horizontal surface using smoke visualization, in temperature driven convection in air at $Pr = 0.7$. The thicker dark lines in the images are the top view of the line plumes. (*a*) $Ra_w = 1.287 \times 10^8$; (*b*) $Ra_w = 1.766 \times 10^8$; (*c*) $Ra_w = 2.183 \times 10^8$; (*d*) $Ra_w = 2.542 \times 10^8$; (*e*) schematic of the large-scale flow in (*a*)–(*d*). The parameters corresponding to the figures are shown in table 1. The planforms and the schematic of figure 4(*e*) show only half the length of the cell.

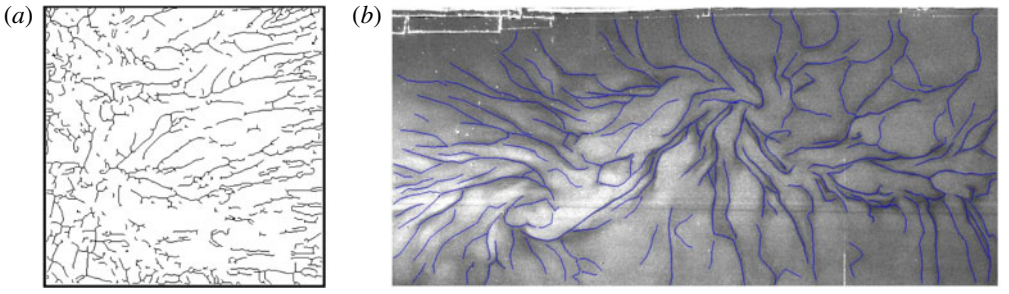

FIGURE 5. (Colour online) (*a*) The negative of the skeletonized image used to calculate the plume length from figure 1(*e*). (*b*) Planform of figure 4(*c*) covered with short linear segments over plume lines for the manual measurement of plume length.

identifies edges in an image where the magnitude of the gradient of the intensity is a local maximum in the gradient direction; such edges should be closed polygons in the present case. In physical terms, this criterion would then imply that a plume edge is detected at the maximum concentration gradient of the fluorescent dye in the PLIF image. In the images at $Pr = 6$ from the electrochemical technique, the plume edges will be detected at the maximum concentration gradient of thymol blue dye. For the $Pr = 0.7$ images we only use the manual detection method where we mark short linear segments on all of the visible plumes in the image. In any case, since the thickness of the plumes do not feature in any part of our analysis, the exact point at which a plume is separated from the background by the algorithm is of no consequence in the final results.

During the edge detection, some regions of the plume edges may not be captured due to the low intensity difference of that region with the background. In such a case, the edge of the plume, that should actually be a closed polygon, could become an unclosed line. Since we use a polygon filling method to mark the plume regions, such unclosed lines would over estimate the plume lengths. To avoid this problem, any edge that had become disconnected from the nearest edge by one pixel due to inaccuracies in the Canny edge detection algorithm was first connected by a bridging routine. To further make the edges closed polygons, we first dilated the image (add one white pixel all around the existing white regions) which further connected any disconnected pixels. An erosion (removal of one pixel from all around the white regions) restored the image back to its original situation except for the points that are connected by the dilation. The closed polygons obtained by this route is then filled with white pixels to obtain plume regions as white pixels over a black background. The peripheral pixels of the white objects in the image were then successively removed until single lines of connected pixels were left behind. An example of the negative of such a skeletonized image corresponding to figure 1(*e*) is shown in figure 5(*a*). The negative image is shown in figure 5(*a*), instead of the actual skeletonized image, so as to clearly see the plume lines captured by this process. The number of white pixels obtained by such a procedure from the skeletonized image, multiplied by the length of a pixel, gives an estimate of the total length of line plumes in the corresponding planform.

The major errors due to the skeletonization were (*a*) missing plumes due to the edges being not detected due to low contrast, (*b*) spurious lines due to bright, non-plume regions in the images, often due to reflections and (*c*) unwanted wiggling of lines when thick plume regions are skeletonized. Owing to these errors the

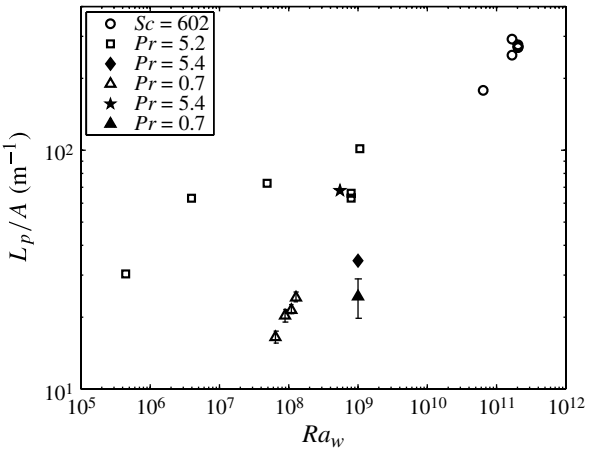

FIGURE 6. Variation of plume length per unit area of the bottom surface with near-wall Rayleigh number (1.1) for $Pr = 0.7$, 5.2 and 602. The filled diamond is the value given by Shishkina & Wagner (2008), the filled star is our measurement from figure 4(*a*) of Zhou & Xia (2010) and the filled triangle is the mean of our measurements from four frames of the movie in Stevens *et al.* (2010).

skeletonization procedure was used only in images with good contrast. In all cases the skeletonized images were visually compared with the original images, and were used only if there was good correspondence of the line pattern with the plume structure. In the case of a not so good correspondence of the line pattern with the plume structure, we used a manual measurement method as described below. Since the manual measurement method is quite accurate, the difference between the measured values of the length of plumes by the two methods, shown later in figure 6, is an estimate of the error involved in the skeletonization procedure.

For the images in figure 4 and for the higher Ra planforms in figure 2, since the skeletonization routine did not capture an appreciable number of plumes, a manual measurement procedure was followed for estimating the length of plumes. For such images, the measurement was performed by using a program that covers the plume lines with short linear segments on mouse clicks over the plume lines, and then calculates the total length of these lines. Figure 5(*b*) shows the planform in figure 4(*c*) covered with such short linear segments, the sum of whose lengths give an estimate of the total length of line plumes. Plume lengths from the images of Stevens *et al.* (2010) and Zhou & Xia (2010) were also measured by this manual method. In the case of Shishkina & Wagner (2008), we used the plume lengths given by them in their table 1.

4. Analysis of plume lengths

A qualitative comparison of the planforms at different Ra_w in figures 1, 2 or 4 show that higher Ra_w results in a denser plume structure at any Pr. The Pr influence on the length of the plumes is not obvious, the effect does not appear to be as strong as that of changing Ra_w. Figure 4(*a*), whose Ra_w is $\approx$2.5 times that of figure 2(*c*), appears to have a similar or even a lower plume density, probably because the Pr is $\approx$10 times lower. However, these visual observations are susceptible to error since the areas of the images are not the same in the figures. There is hence a need to quantify these observations by looking at the variation of the measured plume lengths.

Figure 6 shows the variation of the plume length per unit area L_p/A as a function of Ra_w for $Pr = 0.7$, 5.2 and 602, where L_p is the total length of line plumes that occur over an area A of the bottom plate. Multiple data points at the same Ra_w are due to measurements on the same planform by the two different methods discussed in § 3; these data points give an indication of the error involved in the measurement. For measurements in air at $Pr = 0.7$ the error bars give the standard deviation of the lengths measured from different planforms at the same Ra_w. Figure 6 shows that with increasing Ra_w, larger lengths of plumes occur per unit area of the plate at all Pr. This trend is consistent with the earlier result that the plumes become more closely spaced with increasing Ra_w (PA; TA; Theerthan & Arakeri 2000), which would result in larger number of plumes and hence a larger total length. Larger Ra_w implies larger heat flux, which needs greater length of plumes per unit area to carry away the larger heat flux.

The total length of plumes in the experiments of Zhou & Xia (2010) at $Ra = 1.1 \times 10^9$ and $Pr = 5.4$, measured by us from their figure 4(*a*) using the second method in § 3 is shown as a filled star in figure 6; our measurements from their planforms are consistent with that obtained from our experiments at similar Ra_w and Pr. However, it needs to be pointed out that we identify a greater number of plumes in the planform of Zhou & Xia (2010) as they seem to be counting only the clearer ones of all of the plumes, while we measure the lengths of all of the regions with red colour in their figure 4(*a*). The mean plume length in the numerical simulations of Stevens *et al.* (2010) at $Ra = 2 \times 10^9$ and $Pr = 0.7$ for $\Delta T = 10$ °C, is shown as filled triangle in figure 6. The mean was calculated from our measurements at four dimensionless times from the snapshots of their planforms at a height of $0.0044H$. The associated error bar shows the standard deviation of the data. Comparison of the data of Stevens *et al.* (2010) with our data at the same Pr shows that, considering the error bars, the length in Stevens *et al.* (2010) is approximately consistent with the observation of increased plume lengths with increasing Ra. The plume length given by Shishkina & Wagner (2008) at $Pr = 5.4$, shown as filled diamond in figure 6, seems to be appreciably lower than our experimental measurements at similar Ra_w and Pr.

In figure 6, comparison of the measurements in water and air at the same Ra_w seems to show that a reduction in Pr reduces the plume length per unit area. However, as we show later, such a conclusion will be erroneous and is brought about by looking at the dependence of L_p/A on Ra_w, when the H in the experiments with air is much larger than in the experiments with water. In fact, as we show later, the plume lengths, just like plume spacings, are only dependent on the near-wall variables and is independent of the layer height. We now show that the behaviour of plume lengths in figure 6 could be clearly understood based on relations obtained from two formulations. Both of the formulations have the same underlying assumption that the line plumes are the outcome of the instability of laminar natural convection boundary layers formed on the horizontal surface.

4.1. *Boundary layer formulation*

The mean plume spacing in turbulent convection is given by

$$\overline{\lambda} = C_1 Pr^{n_1} \frac{H}{Ra_w^{1/3}} = C_1 Pr^{n_1} Z_w, \tag{4.1}$$

where

$$Z_w = \left(\frac{\nu\alpha}{g\beta\Delta T_w} \right)^{1/3} = \frac{H}{Ra_w^{1/3}} \tag{4.2}$$

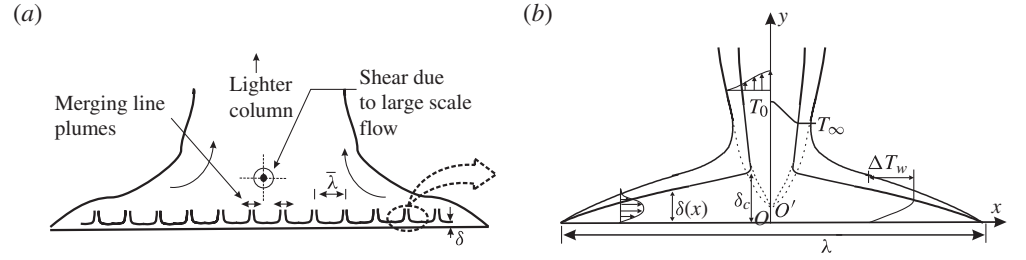

FIGURE 7. A schematic of the assumed phenomenology for the analysis. (*a*) Merging line plumes near the wall result in rising lighter column of fluid that drives the large-scale flow. The large-scale flow causes shear in the direction perpendicular to the plane of the figure thereby aligning the line plumes. (*b*) The magnified view of the region marked with a dashed ellipse in (*a*). Two natural convection boundary layers become unstable at a critical distance of $\bar{\lambda}/2$ when $\delta(x) = \delta_c$ to give rise to a line plume. Here O' is the virtual origin of the plume.

is a near-wall length scale in turbulent convection (Theerthan & Arakeri 2000; TA; PA). A detailed physical explanation of the length scale Z_w in turbulent convection is described in Appendix A. Equation (4.2) was obtained by equating the experimentally observed heat flux relation to the flux carried away from the horizontal surface by laminar natural convection boundary layers over a distance of $\bar{\lambda}$ (TA, PA). The flux carried away by these boundary layers were calculated from the similarity solution of Rotem & Classen (1969). A brief explanation of the procedure used by TA and PA to obtain (4.1) is given in Appendix B. The assumption of natural convection boundary layers on the horizontal surface, that become unstable to give rise to line plumes is inherent in (4.1). A schematic of the assumed boundary layer and plume structure on the horizontal walls is shown in figures 7 and 10(*a*). The model of TA and PA is an extension of the model proposed by Howard (1964) to include the presence of persistent line plumes. Howard (1964) assumed a periodic eruption of a conduction layer to give rise to intermittent thermals.

Given (4.1), a relation that connects $\bar{\lambda}$ to the total length of plumes L_p will give us a relation for L_p in terms of the fluid properties and ΔT_w, which is our objective in the present paper. As per (4.1), $\bar{\lambda} \sim \Delta T_w^{-1/3}$, where the near-wall temperature drop ΔT_w is the same as the temperature drop across the two boundary layers on either side of the plume as well as across the base of each of the line plumes. The plume spacings are dependent on ΔT_w because the thickness at which the boundary layers on each side of the plume becomes unstable to give rise to a plume is given by a relation of the form $Ra_{\delta_c}^{1/3} = a_1 Pr^{b_1}$ (see (4.28)). Here, $Ra_{\delta_c} = g\beta\Delta T_w \delta_c^3/\nu\alpha$ is the Rayleigh number based on the critical boundary layer thickness δ_c at which the boundary layer turns into a plume.

From the results of TA and PA, who obtained $\bar{\lambda}/Z_w = 48$, 53 and 92 for $Pr = 0.7$, 6.0 and 602 respectively, $C_1 = 47.5$ and $n_1 = 0.1$ in (4.1). The estimated uncertainty in C_1 and n_1 is given in Appendix B. Equation (4.1) could also be written in terms of $Ra_\lambda = g\beta\Delta T_w \bar{\lambda}^3/\nu\alpha$, the Rayleigh number based on the mean plume spacing and ΔT_w as

$$\frac{\bar{\lambda}}{Z_w} = Ra_\lambda^{1/3} = C_1 Pr^{n_1}. \tag{4.3}$$

Using the above results, the easiest way to characterize the plume length is to impose a constraint that in an average sense, each individual plume of length L_{pl} will

have a heat transfer area,

$$A_{pl} = L_{pl}\bar{\lambda} \tag{4.4}$$

associated with it. Then,

$$NL_{pl}\bar{\lambda} = NA_{pl} = A, \tag{4.5}$$

where N is the number of individual plumes in an area A of the bottom plate of area A_p. Since the total length of line plumes in area A is

$$L_p = NL_{pl}, \tag{4.6}$$

(4.5) and (4.6) imply that

$$L_p = A/\bar{\lambda}. \tag{4.7}$$

Multiplying both sides of (4.7) with the heat flux Q, it is obvious that (4.7) could also be obtained by assuming that associated with each line plume there are boundary layers on either side of the plume to a distance of $\bar{\lambda}/2$, through which the plume collects the heat from the plate. The area A in (4.7) need not be the total plate area, but any area of the plate over which a plume length of L_p is observed, when $A = A_p$, L_p becomes the total plume length over the bottom plate. The relation (4.7) is also valid for a horizontal surface of arbitrary shape.

Alternatively, if the random plume structure at any Ra and Pr could be replaced by an equivalent array of line plumes spaced at $\bar{\lambda}$ spanning the width W of a region of area A on the bottom plate, purely geometric considerations on the maximum number of plume lines that can be accommodated over the length L of the region imply

$$n = L/\bar{\lambda}. \tag{4.8}$$

In such a case,

$$L_p = nW, \tag{4.9}$$

and (4.8) and (4.9) again imply (4.7). The fact that n and N need not be the same in (4.9) and (4.6) imply that the number of plumes is not a unique parameter to characterize the plume structure since it depends on how we identify individual plumes in a connected plume structure. However, L_p obtained from (4.6) and (4.9) will be the same.

4.1.1. *Rayleigh number relations*

Substituting (4.7) in (4.1) or (4.3), we obtain

$$Ra_p^{1/3} = C_1 Pr^{n_1}, \tag{4.10}$$

where

$$Ra_p = \frac{g\beta\Delta T_w (A/L_p)^3}{\nu\alpha} \tag{4.11}$$

is the Rayleigh number based on A/L_p and ΔT_w. Equation (4.10) is an important relation which shows that the Rayleigh number in terms of the length scale A/L_p remains a constant for a given fluid in turbulent convection. Equation (4.10) is the equivalent relation in terms of L_p to the spacings relation (4.3). Figure 8 shows that the data of figure 6, replotted as $Ra_p^{1/3}Pr^{-n_1}$ is approximately equal to $C_1 = 47.4$ for the three Pr cases, as suggested by (4.10). The plume lengths of Stevens *et al.* (2010) and Zhou & Xia (2010) are also consistent with (4.10). As mentioned earlier, the data

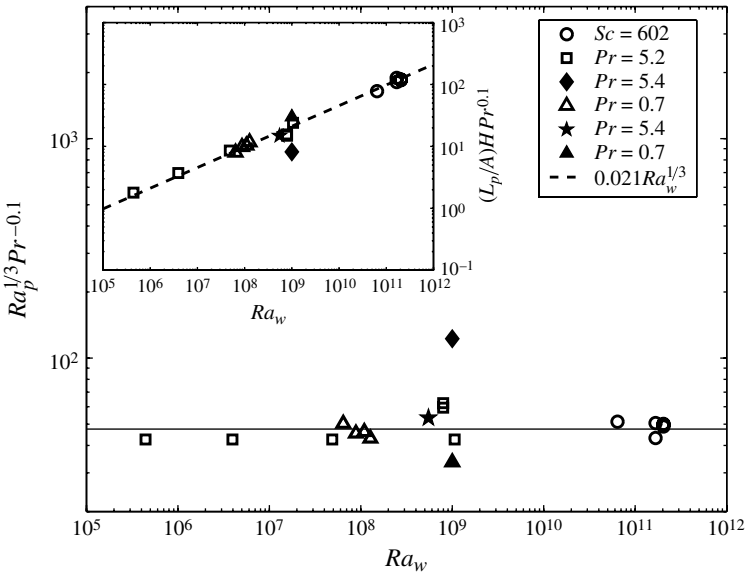

FIGURE 8. Variation of the Rayleigh number based on A/L_p (4.11), normalized by $Pr^{0.1}$, with the near-wall Rayleigh number (1.1). The inset shows that the dimensionless plume lengths L_pH/A scale as $Ra_w^{1/3}$. The filled diamond is the data from Shishkina & Wagner (2008), the filled star that of Zhou & Xia (2010) and the filled triangle is from Stevens *et al.* (2010).

of Shishkina & Wagner (2008) seems to be deviating from (4.10). We presume that this difference is because their chosen threshold, namely the location of the maximum of the thermal dissipation rate, does not capture all of the line plumes.

Equation (4.10) could be rewritten in terms of the plume length normalized by the near-wall length scale A/Z_w as

$$\frac{L_p}{A/Z_w} = \frac{1}{C_1 Pr^{n_1}}, \tag{4.12}$$

implying that the product of the plume length per unit area of the plate and the near-wall length scale Z_w, defined by (4.2), is a constant for a given Pr. Equation (4.12) makes it clear that the plume lengths per unit area are only dependent on the near-wall scales and are independent of the layer height. As per (4.12), increase in Pr reduces the plume lengths per unit area at the same Z_w. The dependence of L_p/A on Pr observed in figure 6, which seems counter to that in (4.12), is due to the different layer heights for the air and water experiments, which will have an effect when L_p/A is studied as a function of Ra_w. The dependence of L_p/A on Ra_w is

$$\frac{Lp}{A/H} = \frac{Ra_w^{1/3}}{C_1 Pr^{n_1}}, \tag{4.13}$$

which shows that the dimensionless plume lengths $L_p/(A/H)$ scale as $Ra^{1/3}$, similar to Nu in turbulent convection. The inset in figure 8 shows this $Ra_w^{1/3}$ scaling of $(L_p/A)HPr^{n_1}$ for all of the fluids.

4.1.2. *Flux relations*

Equation (4.10) relates the plume length per unit area to the driving potential ΔT_w. Similar relations for plume lengths in terms of flux could be obtained from the equivalent relation for spacings in terms of flux,

$$\overline{\lambda} = C_2 Z_o Pr^{n_2}, \tag{4.14}$$

proposed by TA and PA. Equation (4.14) is in terms of

$$Z_o = (\alpha^3/g\beta q)^{1/4} = H/(Nu\,Ra\,Pr)^{1/4}, \tag{4.15}$$

the Townsend's near-wall length scale (Townsend 1959), where $q = Q/\rho C_p$, is the kinematic heat flux. Written in terms of the flux Rayleigh number based on the mean plume spacing $Ra_{\lambda q} = g\beta q\overline{\lambda}^4/\nu\alpha^2 = Nu\,Ra(\overline{\lambda}/H)^4$, (4.14) becomes

$$Ra_{\lambda q}^{1/4} = \frac{\overline{\lambda}}{Z_o Pr^{1/4}} = 31,\ 35 \text{ and } 58 \tag{4.16}$$

for $Pr = 0.7$, 6 and 602 (PA, TA), implying that $C_2 = 31$ and $n_2 = 0.345$ in (4.14).

By substituting (4.7) in (4.14), we get

$$Ra_{qp}^{1/4} = C_2 Pr^{n_3}, \tag{4.17}$$

where

$$Ra_{qp} = g\beta q(A/L_p)^4/\nu\alpha^2 \tag{4.18}$$

is the flux Rayleigh number based on A/L_p and $n_3 = n_2 - 1/4$. Equation (4.17) is an important relation for plume length in terms of flux, similar to (4.10) which is in terms of the driving potential. Figure 9 shows that $Ra_{qp}^{1/4} Pr^{-n_3}$ is equal to $C_2 = 31$ for the three Pr. The plume length per unit area, normalized by Z_o, is

$$\frac{L_p}{A/Z_o} = \frac{1}{C_2 Pr^{n_2}}, \tag{4.19}$$

implying that the product of plume length per unit area and Z_o is a constant for any fluid in turbulent convection. Using (4.10) and the values of n_1 and n_2, (4.19) can be rewritten as

$$Nu = C_3(L_p/A)HPr^{0.08} \tag{4.20}$$

where $C_3 = C_2^4/2C_1^3 = 4.3$. Equation (4.20) gives the expression for the Nusselt number in terms of the plume length per unit area. The inset in figure 9 shows that the experimental variation of $Nu\,Pr^{-0.08}$ with $(L_p/A)H$ for all the fluids match (4.20). Note that (4.20) and (4.13) imply that $Nu = 0.07Ra^{1/3}\,Pr^{-0.02}$, which is very close to the experimentally observed flux scaling by Xia, Lam & Zhou (2002).

4.1.3. *Number of plumes*

Earlier attempts to characterize the plume structure by Zhou & Xia (2010) found that the number of line plumes $N_{pl}^{sheet}/A = 1.4Ra^{0.29\pm0.03}$ (m^{-2}). Even though this equation is likely to be incomplete as it is not dimensionally homogeneous, we could attempt to compare the predictions from the present work with this equation. The number of line plumes predicted by (4.9) and (4.13) is

$$\frac{n}{A} = \frac{Ra_w^{1/3}}{C_1 Pr^{n_1}} \frac{1}{\zeta H^2}, \tag{4.21}$$

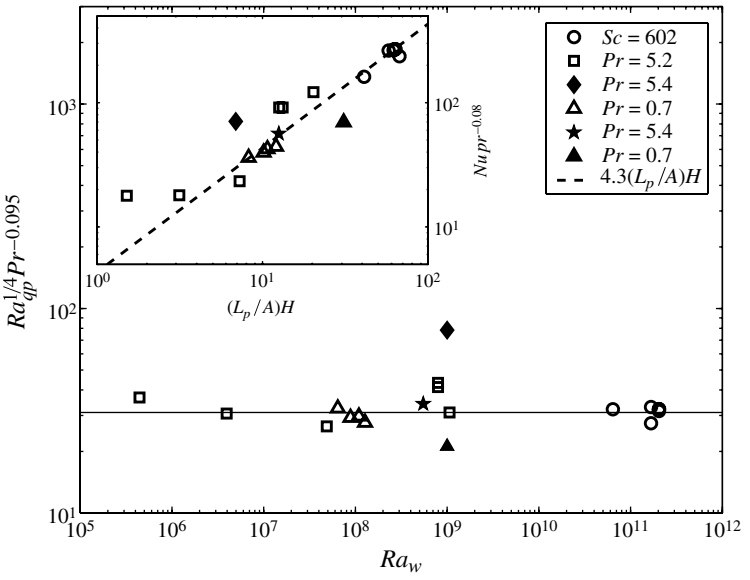

FIGURE 9. Variation of Ra_{qp} the flux Rayleigh number based on A/L_p (4.18), normalized by Pr^{n_3} with Ra_w (1.1). The inset shows the relation of Nusselt number to the plume length per unit area.

which for the experimental values of Zhou & Xia (2010) becomes $n/A = 0.42Ra^{1/3}(m^{-2})$. The dependence of n/A on Ra is consistent with the measurement of Zhou & Xia (2010), but the prefactor is smaller in the present work. This difference is partly because n in (4.21) is the number of plumes spanning the entire width of the plate and is not equal to N_{pl}^{sheet} measured by Zhou & Xia (2010); they also count only the clear plumes. The number of individual plumes per unit area obtained from (4.6) and (4.13) is

$$\frac{N}{A} = \frac{Ra_w^{1/3}}{C_1 Pr^{n_1}} \frac{1}{L_{pl} H} \tag{4.22}$$

which will have an unknown L_{pl}, measuring of which will involve an arbitrary decision to separate out individual plumes from a connected plume structure.

The number of plumes is unlikely to be unique for a given Ra, especially at larger Ra, because the way the plumes are connected depends on factors which often have different values at the same Ra. The most important factor that strongly decides how the plumes are connected is the strength and direction of the large-scale flow. It is well known that the large-scale flow goes through various cessations and reversals at the same Ra (Niemela *et al.* 2001; Ahlers, Grossmann & Lohse 2009). Lower strength of large-scale flow implies that a closed polygon type of plume structure will be formed. In the case of stronger large-scale flow the plumes are often aligned along the large-scale flow direction. If we decide to count the individual plumes as unbranched lines (or lines between corners of the polygon), we will obtain a larger number of plumes in between the reversals than in the presence of a steady large-scale flow, both at the same Ra. It is our experience that the connectedness of the plume structure keeps evolving at a fixed Ra, hence the number of line plumes will also evolve. However since the total heat transported is proportional to L_p and is a weak function of the large-scale flow, L_p remains unique at a given Ra and Pr. The total

number of individual plumes, unlike the total plume length, is unlikely to be unique and is not an appropriate parameter to characterize the plume structure or to relate to the flux scaling. It also needs to be noted that the predictions of the modified theory of Grossman & Lohse (2004) that the total number of line plumes is a constant is quite contrary to the measurements of Zhou & Xia (2010) as well as the present work. All expressions for the plume lengths, derived from (4.3) or (4.17), which were obtained from the assumption of laminar natural convection boundary layers on both sides of the line plumes, agree with the experimental measurements; the near-wall boundary layers in turbulent convection are likely to be laminar natural convection boundary layers.

4.2. *Plume formulation*

The above relations for the plume lengths were obtained from a relation for plume spacings (4.3), in conjunction with a constraint (4.7). This essentially means that the line plumes collect heat from boundary layers spread over a distance of $\bar{\lambda}/2$ on both sides. We now show that similar relations for plume lengths can be obtained by equating the heat carried away by the plumes to the total heat supplied to the plate, along with a stability condition for the laminar natural convection boundary layer. The key assumption, as in the earlier analysis, is that the line plumes very near the walls in turbulent convection are laminar, similar to the plumes studied by Fuji (1963) and Gebhart, Pera & Schorr (1970). These plumes are created by the gravitational instability (Pera & Gebhart 1973) of the laminar natural convection boundary layers between them and carry away most of the heat from the plate. A schematic of such a coherent structure on the horizontal surface is shown in figure 7(*b*). The laminar line plume assumption is justified due to the diffusive nature of the near-wall region where viscosity and thermal diffusivity are important. Further, if the boundary layers between these plumes are laminar natural convection boundary layers, the line plumes that are the outcome of the instability of these boundary layers could be expected to retain their laminar nature for a short distance from the wall. The line plumes are expected to turn turbulent after a short distance from the walls.

For a laminar line plume originating from a horizontal line source, the heat carried away by the plume per unit length of the plume is given by Gebhart *et al.* (1970) as

$$Q_p = 4\mu C_p N \left(\frac{g\beta N}{4\nu^2}\right)^{1/4} I, \tag{4.23}$$

where $\mu = \rho\nu$. $I = \int_{-\infty}^{\infty} f'(\eta_p)\phi(\eta_p)\,\mathrm{d}\eta_p = 1.0331Pr^{-0.486}$ from the results of Gebhart *et al.* (1970). Here f is the dimensionless stream function defined by $\psi = 4\nu(Gr_y/4)^{1/4} f(\eta_p)$ with ψ being the stream function, $'$ indicating differentiation with respect to η_p and

$$\eta_p = \frac{x}{y}(Gr_y/4)^{1/4} \tag{4.24}$$

is the similarity variable for the plume, x is the horizontal coordinate, y the vertical coordinate and the local Grashoff number $Gr_y = g\beta(T_0 - T_\infty)y^3/\nu^2$. The dimensionless temperature difference $\phi = (T - T_\infty)/(T_0 - T_\infty)$ where T is the temperature at any (x, y) location, T_∞ is the ambient temperature and $T_0(y)$ the mid-plane temperature in the plume. N in (4.23) is the prefactor in the power law variation of the plume centre line temperature with y, of the form

$$T_0 - T_\infty = Ny^{-3/5}. \tag{4.25}$$

To find N from (4.25), we need to know the temperature difference across the plume at some height. The temperature difference across the boundary layer is ΔT_w. These boundary layers become unstable and become the plume at the maximum or the critical value of the boundary layer thickness δ_c. Then N could be calculated from (4.25) by assuming the temperature difference across the plume at a height of δ_c is equal to ΔT_w. As shown below, the unknown height δ_c could be estimated from the similarity solution for natural convection boundary layers given by Rotem & Classen (1969) along with a stability condition for such boundary layers.

The similarity solution of Rotem & Classen (1969) gives the thermal boundary layer thickness between the plumes as

$$\frac{\delta(x)}{\bar{\lambda}} = \eta_\delta \left(\frac{x}{\bar{\lambda}}\right)^{2/5} Gr_\lambda^{-1/5}, \tag{4.26}$$

where $Gr_\lambda = Ra_\lambda/Pr$ is the Grashoff number based on $\bar{\lambda}$ and $\eta_\delta = 5Pr^{-1/3}$ is the value at $y = \delta(x)$ of the similarity variable for the boundary layer, $\eta = (y/\bar{\lambda})(x/\bar{\lambda})^{-2/5} Gr_\lambda^{1/5}$. From (4.26), at $x = \bar{\lambda}/2$,

$$\delta|_{x=\lambda/2} = \delta_c = 5 \times 2^{-2/5} \lambda Ra_\lambda^{-1/5} Pr^{-8/15}. \tag{4.27}$$

The stability condition implied by (4.3) and (4.27) is

$$Ra_{\delta_c}^{1/3} = \frac{\delta_c}{Z_w} = \frac{17.7}{\sqrt{Pr}}, \tag{4.28}$$

where $Ra_{\delta_c} = g\beta \Delta T_w \delta_c^3/\nu\alpha$ is the Rayleigh number based on δ_c and ΔT_w. Note that the linear stability analysis of Pera & Gebhart (1973) with a parallel flow assumption predicts the laminar natural convection boundary layers on horizontal surfaces to become unstable at $Ra_\lambda^{1/3} = 245.8Pr^{1/3}$. The experimentally observed spacings are however much smaller, as given by (4.3). We expect this difference to be due to non-parallel flow effects, transient growth and other nonlinearities. We hence use the experimentally observed stability condition (4.3), or the equivalent condition (4.28) for further analysis.

The heat flux from the plate Q is related to Q_p as

$$Q_p L_p = QA. \tag{4.29}$$

Estimating N from (4.25) evaluated at $y = \delta_c$, where $T_0 - T_\infty = \Delta T_w$, the Nusselt number could be estimated using (4.23), (4.28) and (4.29) as

$$Nu = 12.6(L_p/A)HPr^{-0.11}. \tag{4.30}$$

Equation (4.30) has the same dependence on $(L_p/A)H$ as (4.20) but a slightly different Pr dependence and prefactor. We expect these differences to be due to the neglect of the virtual origin of the plume. Here δ_c given by (4.27) is the distance from the horizontal surface. Since the virtual origin considerations will shift the origin of the plume from O on the plate to O' some distance above the plate as shown in figure 7(*b*) (see Appendix B of TA), the distance at which the boundary layer joins the plume, measured in the plume coordinates, will be slightly lower than that given by (4.28), the prefactor will hence reduce. The virtual origin is also a function of Pr, which could account for the slight change in the Pr dependence of (4.30) compared with (4.20). We do not include these considerations here since the second formulation was only to illustrate the consistency of the plume length relations in § 4.1 with the

assumption of laminar natural convection boundary layer giving rise to line plumes as the main near-wall mechanism in turbulent convection.

5. Conclusions

The principal contributions of the present work are the proposed relations for the length of line plumes that form on horizontal surfaces in turbulent convection. The plume length per unit area of the surface (L_p/A) for a given fluid is shown to be inversely proportional to Z_w (4.2), the near-wall length scale in turbulent convection (4.12). This means that for a given fluid, the total plume length in an area A scales as the one-third power of the driving potential, $L_p \sim A\Delta T_w^{1/3}$. This behaviour in turn implies that the Rayleigh number based on the length scale A/L_p is a constant for a given fluid (4.10); the same is true for the flux Rayleigh number based on A/L_p (4.17). The plume length for a given fluid is dependent on the flux Q as $L_p \sim AQ^{1/4}$. In other words, in turbulent convection of a fluid layer of constant height, the plume lengths per unit area on the horizontal surfaces are directly proportional to the Nusselt number (4.20). An increase in the Prandtl numbers results in smaller length of plumes per unit area, but the dependence is weak (4.13). We obtained these relations from the relations for plume spacings (4.1) and (4.14) of TA and PA, who obtained them by equating the heat carried away by laminar natural convection boundary layers over a mean plume spacing $\bar{\lambda}$ to the experimental flux correlations. Similar relations were obtained in § 4.2 when we equated the heat carried away by laminar plumes over their total length L_p on the surface to the total heat input into the plate, along with a stability condition for laminar natural convection boundary layers. The match of these relations with the experimental measurements is a further evidence that the boundary layers in turbulent convection are laminar natural convection boundary layers that become unstable to give rise to line plumes.

We gratefully acknowledge the financial support of DST, Government of India through their grants SR/FST/ETII-017/2003 and SR/S3/MERC/028/2009. B.A.P. and G.S.G. acknowledge the support of DAAD-STAR programme for conducting the $Pr = 0.7$ experiments at DLR, Göttingen. We are grateful to O. Shishkina and C. Wagner for their hospitality at Göttingen.

Appendix A. The physical significance of Z_w

The length scale Z_w is the natural near-wall scale if we assume that buoyancy driven, natural convection boundary layers, which become unstable to give rise to line plumes, are formed on the top and bottom horizontal walls in turbulent convection. The natural convection boundary layer equations, as given by Gill, Zeh & del Casal (1965), Rotem & Classen (1969) and Gebhart *et al.* (1988) are

$$\partial_x u + \partial_y v = 0, \tag{A 1}$$

$$u\partial_x u + v\partial_y u = -\frac{1}{\rho}\partial_x p + \nu\partial_{yy} u, \tag{A 2}$$

$$\frac{1}{\rho}\partial_y p = g\frac{\Delta\rho}{\rho}, \tag{A 3}$$

$$u\partial_x T + v\partial_y T = \alpha\partial_{yy} T. \tag{A 4}$$

Here, u and v are the local horizontal and vertical velocities, p is the local pressure and T the local temperature. We can obtain Z_w by the following order of magnitude

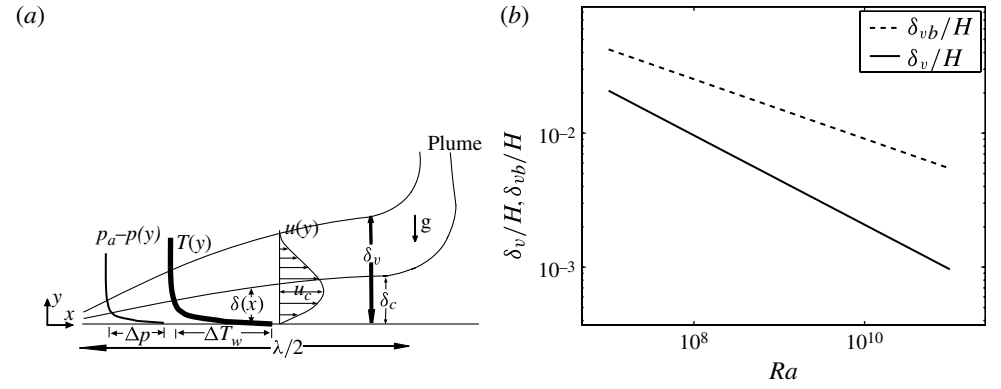

FIGURE 10. (*a*) Schematic of laminar natural convection boundary layer; (*b*) comparison of velocity boundary layer thicknesses for a Prandtl–Blasius boundary layer and a natural convection boundary layer. —, Natural convection velocity boundary layer thickness given by (A 19); - - -, Prandtl–Blasius boundary layer thickness given by (A 23).

balance of (A 1)–(A 4) that characterizes a natural convection boundary layer, a schematic of which is shown in figure 10(*a*).

A.1. *Order of magnitude analysis*

Let L and δ_c be the characteristic length scales in the x and y directions; δ_c is the critical boundary layer thickness as defined in (4.27) and $L = \bar{\lambda}/2$. Let u_c and v_c be the unknown characteristic velocities in the x and y directions, $p_c = \Delta p$ the pressure drop across the boundary layer (see figure 10*a*) be the unknown characteristic pressure and ΔT_w the characteristic temperature difference in the boundary layer. The order of magnitude balance from (A 1) is

$$\frac{u_c}{L} \sim \frac{v_c}{\delta_c}. \tag{A 5}$$

Equation (A 5) implies that the characteristic vertical velocity inside the boundary layer is smaller than the horizontal velocity by a factor of δ_c/L. Similarly (A 3) implies that

$$p_c \sim g\Delta\rho\delta_c. \tag{A 6}$$

The above balance is characteristic of natural convection boundary layers where the horizontal pressure difference due to the density difference between the fluid inside and outside the thermal boundary layer, given by (A 6), drives the horizontal velocities inside the boundary layer. The order of magnitude balance of (A 4) along with (A 5) implies that

$$\frac{v_c\delta_c}{\alpha} \sim 1; \tag{A 7}$$

vertical advection balances diffusion at the edge of the thermal boundary layer. Using (A 5), (A 7) could also be rewritten as

$$u_c \sim \frac{\alpha L}{\delta_c^2}. \tag{A 8}$$

Since (A 8) also implies that $u_c\delta_c/\alpha \sim L/\delta_c$, horizontal advection $\gg$ diffusion at the edge of the thermal boundary layer. Balancing the terms in (A 2) and using (A 5), we obtain

$$\frac{p_c}{\rho u_c^2} + \frac{\nu}{u_c\delta_c}\left(\frac{L}{\delta_c}\right) \sim 1. \tag{A 9}$$

Eliminating p_c from (A 9) using (A 6) and then using (A 8), we obtain

$$Gr_L Pr^2 \left(\frac{\delta_c}{L}\right)^5 + Pr \sim 1, \tag{A 10}$$

where $Gr_L = g\beta\Delta T_w L^3/\nu^2$ is the Grashoff number based on ΔT_w and L.

A.2. *Thermal boundary layer thickness*

Since the force due to the horizontal pressure difference balances the viscous resistance inside the boundary layer, the two terms on the left-hand side of (A 10) should be of the same order, implying

$$\delta_c \sim \frac{L}{(Gr_L Pr)^{1/5}}. \tag{A 11}$$

Equation (A 11) gives the characteristic thermal boundary layer thickness at a horizontal distance L. Equation (A 11) is same as the vertical scale in Rotem & Classen (1969) that is used to stretch the vertical coordinate direction so as to obtain similarity solutions of (A 1) to (A 4). When the horizontal pressure difference due to buoyancy, given by (A 6), balances the viscous resistance in (A 9), the characteristic horizontal velocity obtained is

$$u_c \sim \frac{g\Delta\rho\delta_c^3}{\mu L} \sim \frac{U_{ff}^2}{U_\nu}\frac{\delta_c}{L}, \tag{A 12}$$

where $U_{ff} = \sqrt{g(\Delta\rho/\rho)\delta_c}$ is the free fall velocity over δ_c and $U_\nu = \nu/\delta_c$ is the velocity of viscous diffusion.

For $Pr \sim 1$, (A 11) reduces to

$$\delta_c \sim \frac{L}{Gr_L^{1/5}}; \tag{A 13}$$

all of the following analysis is for moderate Pr using (A 13). Since the boundary layers become unstable at a distance of $\bar{\lambda}/2$ from their leading edge, if we take $L = \bar{\lambda}/2$, (A 13) could be rewritten in terms of Z_w as

$$\delta_c \sim 2^{-2/5}(\bar{\lambda}^2 Z_w^3)^{1/5} Pr^{1/5}, \tag{A 14}$$

implying that the critical thermal boundary layer thickness depends on the two near-wall length scales $\bar{\lambda}$ and Z_w. Since $\bar{\lambda}$ is itself a function of Z_w by (4.1), the critical thermal boundary layer thickness at which the natural convection boundary layer becomes unstable to give rise to a line plume is

$$\delta_c \sim \left(\frac{C_1}{2}\right)^{2/5} Z_w Pr^{2/5}. \tag{A 15}$$

The above relation is for moderate Pr obtained from (A 13); the corresponding relation for large Pr could be obtained from (A 11). The critical thermal boundary layer

thickness and the mean plume spacing are proportional to Z_w, which is hence the relevant near-wall length scale in turbulent convection. Since p_c and u_c are also related to δ_c by (A 6) and (A 12), they can also be written in terms of Z_w.

A.3. *Velocity boundary layer thickness*

Associated with the thermal boundary layers on both sides of the plumes there will also be velocity boundary layers (figures 7*b* and 10*a*), the scaling of its thickness could be found as follows. The velocity boundary layer is dragged by the horizontal motion induced by the density difference in the thermal boundary layer below it. There is hence no force due to a pressure gradient in the velocity boundary layer region above the thermal boundary layer; $p_c = 0$ in (A 9), resulting in

$$\delta_v \sim \sqrt{\frac{\nu L}{u_c}} \sim \frac{L}{\sqrt{Re_b}} \sim \frac{\nu}{U_{ff}} \frac{L}{\delta_c}, \tag{A 16}$$

where the boundary layer Reynolds number, $Re_b = u_c L/\nu$. The velocity boundary layer scales as $1/\sqrt{Re_b}$, as in other theories using Prandtl–Blasius boundary layer. However, the velocity in Re_b is not the large-scale flow velocity, but u_c, obtained by a balance of buoyancy driven pressure gradient and viscous resistance given by (A 12).

Using (A 8) and (A 16), we obtain

$$\frac{\delta_c}{\delta_v} \sim \frac{1}{\sqrt{Pr}}. \tag{A 17}$$

Since δ_c is only a function of Z_w from (A 15), the velocity boundary layer thickness can also be then written in terms of Z_w and Pr as

$$\delta_v \sim \left(\frac{C_1}{2}\right)^{2/5} Z_w Pr^{7/10}. \tag{A 18}$$

Since $Z_w/H = (2/Ra)^{1/3}$, (A 18) can be written in terms of Ra for $Pr \sim 1$ as

$$\frac{\delta_v}{H} \sim 2^{1/3} \left(\frac{C_1}{2}\right)^{2/5} \frac{1}{Ra^{1/3}}. \tag{A 19}$$

A.4. *Comparison with Prandtl–Blasius boundary layer thickness*

It needs to be noted that the velocity boundary layer thickness defined by (A 16) is the thickness of the local velocity boundary layer associated with the laminar natural convection boundary layer of horizontal extent $\bar{\lambda}/2$ on each side of the plume. There will be many such boundary layers, in fact two per plume line, on the whole bottom surface at any given Ra. This velocity boundary layer is different from the Prandtl–Blasius velocity boundary layer assumed to be present in some of the theories of turbulent convection (Grossman & Lohse 2000, 2004). The Prandtl–Blasius boundary layer is expected to be created by the large-scale flow and is assumed to span the entire width of the bottom plate. The thickness of this boundary layer is assumed to follow the well-known relation,

$$\frac{\delta_{vb}}{L} = \frac{0.482}{\sqrt{Re_L}}, \tag{A 20}$$

where

$$Re_L = 0.102\, Ra^{0.447} Pr^{-0.7} \tag{A 21}$$

is the Reynolds number based on the fluid layer width and the large-scale flow velocity (Ahlers *et al.* 2009). The thickness of the Prandtl–Blasius boundary layers could be estimated in terms of Z_w by substituting $Ra = 2(H/Z_w)^3$ in (A 21) and using the resulting expression in (A 20) to obtain

$$\frac{\delta_{vb}}{H} = 1.3\left(\frac{Z_w}{H}\right)^{2/3} Pr^{0.35}, \tag{A 22}$$

for the aspect ratio, $\zeta = 1$. Equation (A 22), in terms of Ra at $Pr \sim 1$ is

$$\frac{\delta_{vb}}{H} = 1.3\left(\frac{2}{Ra}\right)^{2/9}. \tag{A 23}$$

Figure 10(*b*) shows the variation of the velocity boundary layer thickness with Ra given by (A 19) and (A 23), when the boundary layer is of Prandtl–Blasius type and if they are of natural convection type, respectively. The natural convection boundary layer thickness is 2–5 times smaller than the corresponding Prandtl–Blasius boundary layer thickness.

It is possible that a Prandtl–Blasius type boundary layer, caused by the large-scale flow, exists in turbulent convection. However, since the local natural convection boundary layers associated with each plume are much thinner than such forced convection boundary layers due to the large-scale flow, it is unlikely that a Prandtl–Blasius boundary layer will have a major role in the heat transfer. In fact, the reason for the insensitivity of Nu to the large-scale flow strength, found by many researchers (see § F in Ahlers *et al.* 2009), could be the presence of these thinner local natural convection boundary layers, whose thickness essentially decides the heat flux in turbulent convection.

Appendix B. Uncertainty in the plume spacing relation (4.1)

The accuracy of the proportionality constant C_1 and the power law exponent n_1 in (4.1) decides the accuracy of most of the results in the present work. All of the results in terms of the driving potential in § 4.1.1 are obtained from (4.1). Similarly, all of the results in terms of the flux in § 4.1.2 are obtained from (4.14) that has another proportionality constant C_2 and a power law exponent n_2. However, since the flux Rayleigh number based on the mean plume spacing

$$Ra_{\lambda q} = 2^{4/3} a\, Pr^b Ra_\lambda^{4/3}, \tag{B 1}$$

when $Nu = aRa^{1/3}Pr^b$, C_1 and C_2 are related by

$$C_2 = 2^{1/3} a^{1/4} C_1 \quad \text{and} \quad n_2 = n_1 + (b-1)/4. \tag{B 2}$$

Hence, an estimate of the accuracy of C_1 and n_1 clarifies the accuracy of all of the other pre-factors and exponents in the present work. Further, since (4.1) was obtained from the results of TA and PA, we include an explanation of how (4.1) was obtained to make the present work self-contained.

Equation (4.1) was obtained by TA as follows. The expression for Nu, obtained from the average heat flux over a length of $\bar{\lambda}$ calculated using the similarity solution of Rotem & Classen (1969) for natural convection boundary layers, is

$$Nu = \frac{-5 \times 2^{1/15}}{6} H'(0) Ra_\lambda^{-2/15} Pr^{-1/5} Ra^{1/3}, \tag{B 3}$$

where $H'(0) = 0.3826Pr^{0.2692}$ from Rotem & Classen (1969). If (B 3) is equated to a correlation for Nu we obtain an expression for $\overline{\lambda}/Z_w$. TA used the correlation of Globe & Dropkin (1959),

$$Nu = a\,Ra^{1/3}\,Pr^{b}, \tag{B 4}$$

where $a = 0.069$ and $b = 0.074$ in the range $1.51 \times 10^5 \leqslant Ra \leqslant 6.76 \times 10^8$ and $0.02 \leqslant Pr \leqslant 8750$ to obtain

$$Ra_\lambda^{1/3} = 52Pr^{-0.012}. \tag{B 5}$$

From (B 5), $C_1 = 52$ and $n_1 = -0.012$ which are different from the values of $C_1 = 47.5$ and $n_1 = 0.1$ used in the paper, especially the Pr dependence. However (B 4) itself shows a large variation of a and b, with the latest experiments conducted in a wide range of Pr by Xia *et al.* (2002) giving

$$Nu = 0.14Ra^{0.297}\,Pr^{-0.03}, \tag{B 6}$$

in a range $2 \times 10^7 \leqslant Ra \leqslant 3 \times 10^{10}$ and $4 \leqslant Pr \leqslant 1350$. If we substitute (B 6) instead of (B 4) in (B 3), we obtain

$$Ra_\lambda^{1/3} = 8.79Ra^{0.09}\,Pr^{0.248}. \tag{B 7}$$

Now $26 < C_1 < 91$ for $2 \times 10^5 < Ra < 2 \times 10^{11}$ and $n_1 = 0.25$. So, in essence, the uncertainty in C_1 and n_1 is the uncertainty present in the flux correlations.

One can also obtain (4.1) without using flux correlations by using a relation between Ra_λ and Ra_{δ_c}, the Rayleigh number based on the critical boundary layer thickness at which the boundary layer turns into a plume. This relation, as derived from the similarity solution of Rotem & Classen (1969) by TA is

$$Ra_\lambda = 8Ra_{\delta_c}^{5/2}\eta_\delta^{-15/2}Pr^{-3/2}, \tag{B 8}$$

where $\eta_\delta = 5Pr^{-1/3}$ is the value of the similarity variable of Rotem & Classen (1969) at the boundary layer edge. If we now have a condition for the instability of the boundary layer in terms of Ra_δ we will be able to obtain an expression for Ra_λ independent of the flux correlations. The only available instability analysis of natural convection boundary layers on horizontal surfaces is by Pera & Gebhart (1973), which gives $Ra_{\delta_c}^{1/3} = 34$. The corresponding plume spacing relation will then be $Ra_\lambda^{1/3} = 245.8Pr^{1/3}$ which is much larger than the experimentally verified relation (4.3). We expect this difference to be due to the parallel flow assumption used in the stability analysis of Pera & Gebhart (1973).

Hence, we conclude that the form of the power law relation (4.1) is certain from the analysis of TA and PA, even though there is uncertainty in the coefficients due to the uncertainties in flux correlations or due to the approximations in the stability analysis. In view of such a situation, we estimated C_1 and n_1 as follows. Numerical simulations by TA at $Pr = 0.7$ and 6 gave $Ra_\lambda^{1/3} = 48$ and 53. Analysis by PA using the infinite Pr similarity solutions of Rotem & Classen (1969) gave $Ra_\lambda^{1/3} = 92$ for $Sc = 602$, these relations matched the measurements of Theerthan & Arakeri (2000) and PA. We hence used a power law fit between the above three values of $Ra_\lambda^{1/3}$ at $Pr = 0.7$, 6 and 602 to obtain (4.1).

Figure 11 shows the values from TA and PA, along with the curve fit (4.1) through them. The estimated error range for the prediction of (4.1) is shown as the error bars. Power law fits through the maximum range of variation of (4.1) are shown as the

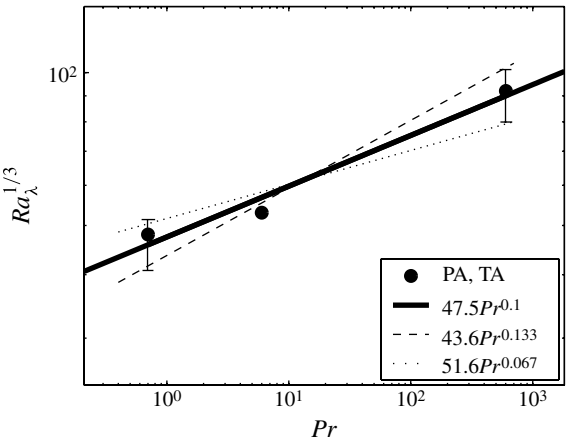

FIGURE 11. Uncertainty in the curve fit $\overline{\lambda}/Z_w = Ra_\lambda^{1/3} = C_1 Pr^{n_1}$ (4.1).

dotted and the dashed lines. Using these error estimates, (4.1) could be written as

$$\frac{\overline{\lambda}}{Z_w} = 47.5 \pm 4 Pr^{0.1 \pm 0.033}. \tag{B 9}$$

REFERENCES

ADRIAN, R. J., FERREIRA, R. T. D. S. & BOBERG, T. 1986 Turbulent thermal convection in wide horizontal fluid layers. *Exp. Fluids* **4**, 121–141.

AHLERS, G., GROSSMANN, S. & LOHSE, D. 2009 Heat transfer and large-scale dynamics in turbulent Rayleigh–Bénard convection. *Rev. Mod. Phys.* **81**, 503.

BAKER, J. D. 1966 A technique for the precise measurement of small fluid velocities. *J. Fluid Mech.* **26** (3), 573–575.

CANNY, J. 1986 A computational approach to edge detection. *IEEE Trans. Pattern Anal. Mach. Intell.* **8** (6), 679–698.

FUJI, T. 1963 Theory of the steady laminar natural convection above a horizontal line source and a point heat source. *Intl J. Heat Mass Transfer* **6**, 597–606.

FUNFSCHILLING, D. & AHLERS, G. 2004 Plume motion and large scale circulation in a cylindrical Rayleigh–Bénard cell. *Phys. Rev. Lett.* **92** (19), 194502.

GEBHART, B., PERA, L. & SCHORR, A. W. 1970 Steady laminar natural convection plume above a horizontal line heat source. *Intl J. Heat Mass Transfer* **13**, 161–171.

GEBHART, B., JALURIA, Y., MAHAJAN, R. L. & SAMMAKIA, B. 1988 *Buoyancy Induced Flows and Transport*. Hemisphere Publishing.

GILL, W. N., ZEH, D. W. & DEL CASAL, E. 1965 Free convection on a horizontal plate. *Z. Angew. Math. Phys.* **16**, 532–541.

GLOBE, S. & DROPKIN, D. 1959 Natural-convection heat transfer in liquids confined by two horizontal plates and heated from below. *Trans. ASME*, 24–28.

GROSSMAN, S. & LOHSE, D. 2000 Scaling in thermal convection: a unifying theory. *J. Fluid Mech.* **407**, 27.

GROSSMAN, S. & LOHSE, D. 2004 Fluctuations in turbulent Rayleigh Bénard convection: the role of plumes. *Phys. Fluids* **16**, 4462–4472.

GUNASEGARANE, G. S. & PUTHENVEETTIL, B. A. 2010 Merging of sheet plumes in turbulent convection. In *Proceedings of the 37th National and the 4th International Conference on Fluid Mechanics and Fluid Power* (ed. B. V. S. S. Prasad). IIT Madras, Chennai, India, ISBN 978-81-910571-1-9, Valardocs, Chennai.

HARAMINA, T. & TILGNER, A. 2004 Coherent structures in boundary layers of Rayleigh–Bénard convection. *Phys. Rev.* E **69**, 056306.

HOWARD, L. N. 1964 Convection at high Rayleigh number. In *Proceedings of the 11th International Congress Applied Mechanics, Munich* (ed. H. Görtler), pp. 1109–1115.

HUSAR, R. B. & SPARROW, E. M. 1968 Patterns of free convection flow adjacent to horizontal heated surfaces. *Intl J. Heat Mass Transfer* **11**, 1208–1211.

NIEMELA, J. J., SKRBEK, L., SREENIVASAN, K. R. & DONNELY, R. J. 2001 The wind in confined thermal convection. *J. Fluid Mech.* **449**, 169–178.

PERA, L. & GEBHART, B. 1973 On the stability of natural convection boundary layer flow over horizontal and slightly inclined surfaces. *Intl J. Heat Mass Transfer* **16**, 1147–1163.

PUTHENVEETTIL, B. A., ANANTHAKRISHNA, G. & ARAKERI, J. H. 2005 Multifractal nature of plume structure in high Rayleigh number convection. *J. Fluid Mech.* **526**, 245–256.

PUTHENVEETTIL, B. A. & ARAKERI, J. H. 2005 Plume structure in high Rayleigh number convection. *J. Fluid Mech.* **542**, 217–249.

PUTHENVEETTIL, B. A. & ARAKERI, J. H. 2008 Convection due to an unstable density difference across a permeable membrane. *J. Fluid Mech.* **609**, 139–170.

RAMAREDDY, G. V. & PUTHENVEETTIL, B. A. 2011 The $Pe \sim 1$ regime of convection across a horizontal permeable membrane. *J. Fluid Mech.* **679**, 476–504.

ROTEM, Z. & CLASSEN, L. 1969 Natural convection above unconfined horizontal surfaces. *J. Fluid Mech.* **39** (part 1), 173–192.

SHISHKINA, O. & WAGNER, C. 2007 Local fluxes in turbulent Rayleigh–Bénard convection. *Phys. Fluids* **19**, 085107.

SHISHKINA, O. & WAGNER, C. 2008 Analyis of sheet-like thermal plumes in turbulent Rayleigh–Bénard convection. *J. Fluid Mech.* **599**, 383–404.

STEVENS, R. J. A. M., VERZICCO, R. & LOHSE, D. 2010 Radial boundary layer structure and Nusselt number in Rayleigh Bénard convection. *J. Fluid Mech.* **643**, 495–507.

TAMAI, N. & ASAEDA, T. 1984 Sheet like plumes near a heated bottom plate at large Rayleigh number. *J. Geophys. Res.* **89**, 727–734.

THEERTHAN, S. A. & ARAKERI, J. H. 1998 A model for near wall dynamics in turbulent Rayleigh–Bénard convection. *J. Fluid Mech.* **373**, 221–254.

THEERTHAN, S. A. & ARAKERI, J. H. 2000 Plan form structure and heat transfer in turbulent free convection over horizontal surfaces. *Phys. Fluids* **12**, 884–894.

TOWNSEND, A. A. 1959 Temperature fluctuations over a heated horizontal surface. *J. Fluid Mech.* **5**, 209–211.

XIA, K. Q., LAM, S. & ZHOU, S. Q. 2002 Heat flux measurement in high Prandtl number turbulent Rayleigh–Bénard convection. *Phys. Rev. Lett.* **88** (6), 064501.

ZHOU, Q., SUN, C. & XIA, K. Q. 2007 Morphological evolution of thermal plumes in turbulent Rayleigh–Bénard convection. *Phys. Rev. Lett.* **98**, 074501.

ZHOU, Q. & XIA, K. Q. 2010 Physical and geometrical properties of thermal plumes in turbulent Rayleigh Bénard convection. *New J. Phys.* **12**, 075006.

ZOCCHI, G., MOSES, E. & LIBCHABER, A. 1990 Coherent structures in turbulent convection, an experimental study. *Physica* A **166**, 387–407.